DOI:
10.1039/d1nr01251g

Document Version
Peer reviewed version

ARTICLE

Directional imbalance of Bloch surface waves for ultrasensitive displacement metrology

Ruxue Wang[ab, ‡], Xinrui Lei[cd, ‡], Yi Jin[e], Xiaolei Wen[f], Luping Du[c*], Aimin Wu[ab,*], Anatoly V. Zayats[d], Xiaocong Yuan[c]

Precise position sensing and nanoscale optical rulers are important in many applications in nanometrology, gravitational wave detection and quantum technologies. Several implementations of such nanoscale displacement sensors have been recently developed based on interferometers, nanoantennas, optical field singularities and optical skyrmions. Here, we propose a method for ultrasensitive displacement measurements based on the directional imbalance of the excitation of Bloch surface waves (BSWs) by an asymmetric slit, which have low propagation loss and provide high detected intensity. The directionality of the excitation changes dramatically with a sub-nanometric displacement of the illuminating Gaussian beam across the slit and can be used for displacement and refractive index metrology. We demonstrate a theoretical intensity ratio of the BSW excitation in opposite directions exceeding 890, which provides the displacement sensitivity up to 2.888 nm^{-1} with a resolution below 0.5 nm over the 100 nm linearity range. Experimentally, a directional intensity ratio more than 90 has been achieved, with a displacement sensitivity of 0.122 nm^{-1} over a 300 nm linearity range, resulting in a resolution below 8 nm for a 600 nm illumination wavelength. The proposed facile configuration may have potential applications in nanometrology and super-resolution microscopy.

Introduction

Optical metrology and position sensing techniques play a key role in many areas of modern science and technology from gravitational wave detection to sensing of conformational changes of molecules and scanning probe microscopy.[1-3] Optical techniques are of great importance to provide noncontact capabilities, despite optical resolution is limited by diffraction. Deep-subwavelength displacement sensing has been demonstrated using active, such as Forster resonant energy transfer or second-harmonic generation,[4-7] and passive approaches. In addition to conventional macroscopic interferometers suitable for longitudinal displacement measurements and requiring high stability lasers,[8, 9] other approaches are based on directional scattering from nanoantennas using near-field interference,[10] localized plasmonic resonances,[11, 12] electromagnetic field singularities[13-16] and optical skyrmions,[17] to name but a few. While providing sub-nm resolution in displacement detection, these approaches, however, rely on the detection of scattering from various types of nanoantennas, demanding high accuracy of either the nanostructure or optical field when receiving a weak detected signal. This poses the demands on the sophisticated detection systems to remove background and improve signal-to-noise ratio. The sensitivity of these methods is also highly nonlinear with a limited working distance range (usually less than 50 nm for 0.05 nm^{-1} sensitivity) since high displacement sensitivity exists only near the locations of optimal directionality.

The directional excitation of surface plasmon polaritons (SPPs), including the approaches based on nano-antennas exciting SPPs with high unipolar directionality[18-22] and polarization-controlled directionality of SPPs,[23, 24] has also potential for metrology applications. The intrinsic nonradiative loss of SPPs, however, limits their application in metrology. Recently, the use of Bloch surface waves (BSWs) excited at the surface of a truncated periodic dielectric multilayer has been proposed to circumvent the intrinsic metallic loss in plasmonics. As a prominent counterpart to SPPs, BSWs exist on dielectric multilayers which can be fabricated on a CMOS material platform,[25-27] have low propagation loss[28, 29] and may support both TE and TM modes.[30] The free top surface of the BSW devices and the high field localization allows for sensing applications,[31-33] possibility of strong coupling to organic emitters,[34] and different kinds of surface patterning such as for grating couplers and splitting elements.[35, 36] On the other hand, dielectric nano-antennas have potential to provide tools for the manipulation of BSWs on the interface[37-41] and may open up new approaches for ultrasensitive displacement and position metrology.

In this paper, we propose a novel approach for high-precision translational displacement sensing based on directional imbalance of the BSWs generated by nanoantennas. First, by analyzing the scattering behavior of an exciting free-space plane wave and the excited BSWs on the nanoslits in the dielectric multilayer, we optimize the geometry of nanoslits to achieve highly unidirectional excitation of BSWs. Due to the unique dispersion relation of BSWs, the directional extinction ratio R— the ratio of the intensities of the BSWs propagating in

opposite directions—which is sensitive to the wavelength of the incident light, can theoretically reach up to 890 (29.5 dB) and has been experimentally measured to be more than 90 (19.5 dB), limited by roughness and fabrication uncertainties. The strong unidirectionality gives rise to highly precise displacement sensing under illumination with a loosely focused (NA<0.2) free space Gaussian beam or in the case of illumination with an optical fiber. We theoretically demonstrate that *R* varies linearly for sub-nanometric displacements of the slits (or a beam) over 100 nm range with a sensitivity (the variation of *R* per nanometer) of 2.888 nm^{-1} and a resolution of below 0.5 nm for the illumination wavelength of 600 nm. The linearity range was experimentally verified to reach 300 nm with a uniform sensitivity of 0.122 nm^{-1}, reduced, compared to the theoretical estimates, due to the sample fabrication imprecision and the noise in the acquisition system. In comparison to the approaches using resonance nanoparticles[14-16], the accuracy of data processing can be greatly increased by the strong scattering signal of the BSW, reducing acquisition time and, therefore, the role of environmental vibrations. The facile configuration for precision displacement measurements may have potential applications in optical nanometrology, localization microscopy, and lithography mask alignment.

Results and discussion

Bloch surface waves and their excitation

Bloch surface waves were excited on the dielectric multilayer (18 layers) consisting of alternating layers of SiO_2 (low refractive index, n=1.46+i10^{-5}) and SiN_x (Si Rich, high refractive index, n=2.74 at a wavelength of 600 nm but highly dispersive) on a cover glass. The thicknesses of the alternating SiO_2 and SiN_x layers are 100 and 80 nm, respectively, and the thickness of the top SiO_2 is 390 nm (Fig. 1a). The photonic band structure of the studied dielectric multilayer for the TM modes is shown in Fig. 1b. The white zones correspond to the photonic forbidden band of the dielectric multilayer, where the Bloch wave numbers are imaginary and surface wave can exist, while the black zones denote the allowed photonic bands, where light can propagate inside the multilayer. The TM-polarized surface mode is supported in the wavelength range of 580 to 680 nm (red solid line in Fig. 1b, calculated via the transfer matrix method[42]).

A nanoslit etched in the multilayer structure acts as a nanoantenna which couples an incident free-space beam to BSWs propagating on a surface of the multilayer. The SPP coupling efficiency has been shown to have an oscillating dependence on the slit width and depth.[22, 43] The relation between the slit width and the BSW coupling efficiency has a similar oscillatory dependence due to the diffractive origin of surface wave generation.[44] However, the dependence on the slit depth is expected to be different for BSW than for SPPs. In the latter case, the coupling is related to the Fabry–Perot modes in the cavity formed by the metal/air/metal structure with refractive indices independent of the slit depth (assuming the metal is thick enough).[45] In the case of BSWs, the thickness of the top layer determines the location of the dispersion line in the band gap.[42] Consequently, an effective refractive index seen by BSW depends on the slit depth (Fig. 1c) and a more complicated dependence of the excitation efficiency on the slit depth is observed (Fig. 1d). Numerical simulations were performed by finite difference time domain (FDTD) method to understand the excitation process of BSWs. Under normally incident plane wave illumination, photon-BSW coupling can be quantified by the coupling efficiency η, denoting the electric field amplitude ratio between the excited BSW and the incident light, as well as the coupling phase φ, representing the initial phase of the excited BSW. The efficiency and phase variations with the slit width and depth are shown in Figs. 1d and e for a wavelength of 600 nm (assuming that the transverse length is infinite for both slit and the plane wave). With increasing slit depth in the top layer, the coupling efficiency increases rather than oscillating with the half-wavelength period, as typically observed for SPPs excited by a slit in a metal film.[22, 46]

The described behavior of BSWs excitation by the slit gives rise to the asymmetric excitation of BSWs when introducing two slits with different width and depth. The schematic diagram to realize asymmetric excitation is shown in Fig. 2a. Labeling the coupling amplitude (product of amplitude of incident light and coupling efficiency, ηE_{in}) and phase of the launched BSWs at 'slit-1' and 'slit-2' as E_1, φ_1 and E_2, φ_2, respectively, the BSW field propagating along the $\pm x$ directions can be expressed as $E_+ \propto E_2 e^{i\varphi_2} + E_1 e^{i(\varphi_1 + k_{BSW} d)} t_2^*$ and $E_- \propto E_1 e^{i\varphi_1} + E_2 e^{i(\varphi_2 + k_{BSW} d)} t_1^*$, respectively, where d is the distance between the centers of the two slits and $t_i^* = t_i \varphi_{it}$ (i=1,2) is the complex transmission coefficient for the BSW crossing 'slit i' (i=1,2) when passing through another slit. Different from the previous work on SPPs,[22, 46] the transmission of BSWs by a nanoslit has a non-negligible contribution due to the excitation of the mode inside the slit, which will introduce an additional phase to the electric field for both sides of the slit. To achieve destructive interference on one side of the double slit, the negative x-axis for instance, φ_1 and $\varphi_2 + k_{BSW} d + \varphi_{2t}$

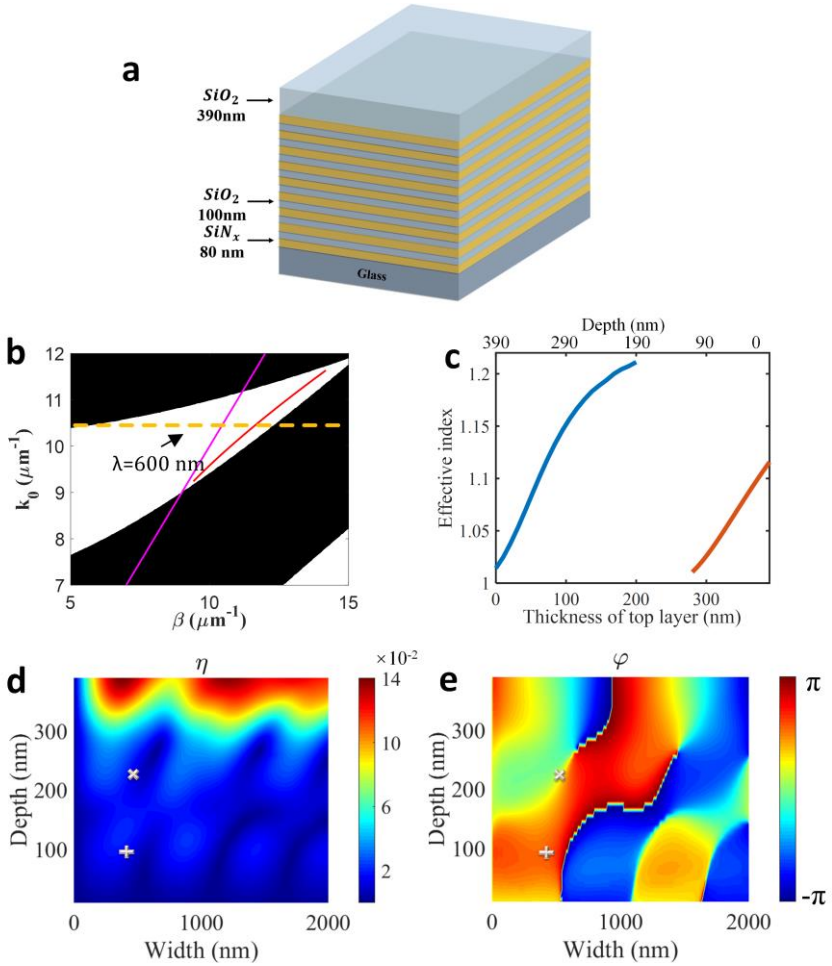

Fig. 1 Bloch surface waves and their excitation by a single nanoslit. (a) Schematic illustration of a dielectric multilayer structure supporting BSW. (b) Simulated photonic band structure of the dielectric multilayer for TM polarized modes. The white regions correspond to the photonic forbidden bands, where light cannot propagate through the multilayer, and the black regions represents the allowed bands. The red solid line denotes the dispersion curve for the BSW. The purple line denotes the light line in vacuum. The yellow dotted line indicates a wavelength of 600 nm considered in (c-e). The parameters of the structure are as in (a). (c) Variation of the effective index of the BSW modes at a vacuum wavelength of 600 nm with thickness of the top layer. Two different TM-BSW modes exist in the considered thickness range, where the blue line denotes TM_0-BSW and red line denotes TM_1-BSW, respectively. (d-e) Dependence of (d) coupling efficiency η and (e) coupling phase φ of the BSW on the slit width and depth for a wavelength of 600 nm. The markers '+' and '×' denote the dimensions of the asymmetric slits considered in Fig 2.

should be π out of phase, which is the basis for the unidirectional excitation of BSWs. To make the extinction ratio as large as possible, for positive *x*-axis, φ_2 and $\varphi_1 + k_{BSW}d + \varphi_{1t}$ should be in phase at the same time. Thus, BSWs propagating in the negative direction of the *x*-axis will be suppressed by destructive interference, whereas constructive interference will occur on the other side.

Neglecting the phase acquired by the BSW going through the slit, unidirectional excitation can be achieved in a straightforward manner when $\Delta\varphi = \varphi_2 - \varphi_1 = k_{BSW}d = (N + 1/2)\pi$. The coupling phase difference between the two slits $\Delta\varphi = \varphi_2 - \varphi_1 = \pi/2$ can be maintained if the distance between the slits is chosen to compensate the phase acquired upon transmission through the slits. In order to achieve this, we select the widths and depths of the slits as w_1=530 nm, h_1=230 nm and w_2=400 nm, h_2=90 nm, which give $\eta_1 \approx \eta_2 \sim 1\%$, $\Delta\varphi \approx \pi/2$ as can be estimated from Figs. 1d–e. To achieve directional coupling with highest possible extinction ratio in the opposite directions and a minimal size, the coupling efficiency is compromised and not as high as that with periodic slit or hole arrays.[32, 33, 47] If we vary the distance between the centers of the slits, the variation of the amplitude on each side of the double slit follows approximately a sine function with a distinct phase shift, and the maximum extinction ratio indicating the unidirectionality is achieved at an optimal distance of *d*=755 nm (Fig. S1). The resultant near-field distribution of E_z under the normal plane-wave illumination (Fig. 2b) indeed shows a BSW propagating in +*x* direction with a much greater amplitude than the one propagating in −*x* (extinction ratio *R*=400). The asymmetric far-field emission due to the outcoupling of the BSWs in the far field has a pronounced directionality (Fig. 2c). It is worth noting that this mechanism to obtain directionality may also be applied to dielectric and SPP waveguides.

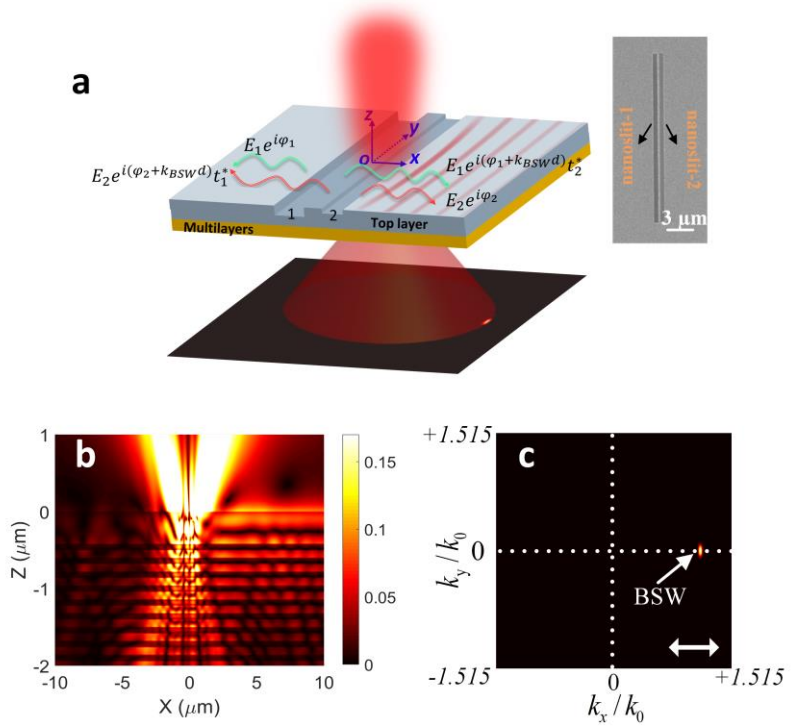

Fig. 2 Unidirectional excitation of BSWs with an asymmetric double slit. (a) Schematics of the unidirectional excitation of BSWs by an asymmetric double slit. Below the multilayer, the angular spectrum of the excited BSWs is presented as a schematic. The origin of the coordinate axis is denoted by 'o' at the center of the SiO_2 ridge between the slits. The inset is a top-view SEM image of the asymmetric double slit in the top layer. (b) Simulated near-field distribution of the electric field E_z in *x*-*z* plane across the multilayer. The central vertical dark fringe arises from the destructive interference of the scattering fields from the two slits, which have opposite propagating direction along *x* axis, resulting in π out of phase between E_z generated by the two slits. (c) Simulated far-field angular spectrum of the BSWs excited by an asymmetric double slit under the illumination with a normally incident TM-polarized plane wave. The white double arrow denotes the polarization. The parameters of the multilayer are as in Fig. 1c. The width and depth of the slits are w_1=530 nm, h_1=230 nm, w_2=400 nm, h_2=90 nm, and the separation between the slits 755 nm (centre to centre). The illuminating light wavelength is 600 nm.

Experimental demonstration of asymmetric excitation of BSW

We experimentally demonstrated directional BSW excitation with the leakage radiation observations (Fig. S2).[48, 49] The depth of each slit and distance between the slits in the fabricated sample correspond to the designed values (Fig. S3g), while the cross sectional shape is trapezoid with the full widths at half maximum (FWHM) corresponding to the designed slit width (see Methods and Fig. S3 for the details of fabrication). The simulated and experimental back focal plane (BFP) images obtained under the illumination with a Gaussian beam (NA=0.17) at the wavelengths of 580, 600, 630, and 650 nm are shown in Figs. 3a-h. The BSW propagation length at a wavelength of 600 nm was estimated from the corresponding real space images (Fig. S4a) to be approximately 15.3 μm. Since we are mainly interested in the BSW behaviour, the incident Gaussian beam and other scattered light were numerically filtered with data post-processing to make the directional behavior clear (see Methods for the details of the post-processing; raw and post-processed images are shown in Figs. S4b and c). The BFP images of reflected white light were also measured in order to derive the wavenumbers of the BSWs at these wavelengths (Figs. S4d-g), which correspond to 1.16 k_0, 1.115 k_0, 1.063 k_0, and 1.022 k_0 for the mentioned above wavelengths, consistent with the dispersion of the BSWs (Fig. 1b). The collection objective NA=1.49 limits the highest accessible wavenumber $|k_{\parallel}/k_0| \leq 1.49$. The directional intensity ratio of the excited BSW can be calculated as $R = I_r / I_l$, where I_l and I_r are the total intensities of the BSWs in the opposite directions in *k* space with $|\Delta k_x| < 0.015k_0$, which approximately equals the full width at half maximum of the BSW peak and $|\Delta k_y| < 0.1k_0$, integrating the BSW intensity in the *y* direction.

The maximum *R* was obtained to be 400 in the simulations and around 70 in the experiment at a wavelength of 600 nm and decreased sharply for other wavelengths, indicating a high spectral sensitivity of the directionality (Figs. 3i-j) due to the rapid changes of a BSW wave vector with wavelength (Fig. 1b). Varying a wavelength while keeping a fixed distance between the two slits introduces an extra phase, which modifies constructive and destructive interference on different sides of the double slit, decreasing the extinction ratio. The variation of a wavelength also induces a non-negligible change of the excited BSW, leading to a rapid decrease of *R* away from the optimal wavelength. The discrepancy in the experimental and simulated extinction values arises from the variations in shape and smoothness of the slits. The roughness and thickness variation over the sample area, which accumulates with the increase of the number of layers (Fig. S3a), leads to unwanted scattering of surface waves and introduces a tilt of the incident beam with respect to the nanostructure. The trapezoid shape of the fabricated slits (Figs. S3f and g) also influences the extinction

ratio (see Methods and Fig. S5 for details). These fabrication uncertainties result in the deviations between the experimental and simulated results. The observed high sensitivity to wavelength could be potentially used for spectroscopic applications.

extinction ratio *R* can be expressed via the interference fields of the BSWs excited by each slit:

$$R = \frac{E_{1e}^2 + E_{2e}^2 + 2E_{1e}E_{2e}\cos\Delta\phi_0}{E_{1e}^2 + E_{2e}^2 + 2E_{1e}E_{2e}\cos\Delta\phi_\pi}, \quad (1.)$$

where $\Delta\phi_0$ is the phase required for constructive interference

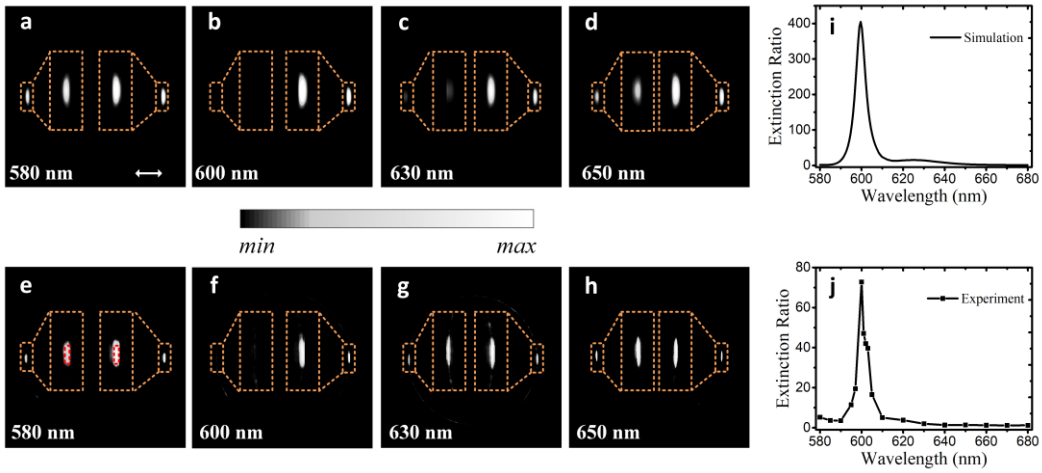

Fig. 3 Wavelength dependence of the directional BSW excitation. (a-d) Simulated and (e-h) experimental BFP images of the BSWs for different wavelengths. White double arrows in (a) indicate the polarization of the incident Gaussian beam (NA=0.17). The insets on the two sides of the main images show the enlarged views marked by the orange rectangles with the BSW signal. The red dotted rectangles in (e) represent the BSW intensity integration area for the evaluation of the extinction ratio. The maximum of the greyscale for (a-h) is slightly overexposed to increase visibility of the spots on the left; please see the absolute values of the extinction ratios in (i,j). (i) Simulated and (j) experimental wavelength dependence of the directional extinction ratio *R*.

Displacement metrology based on asymmetric excitation of BSW

The developed above photonic system can be applied for metrology applications as follows. If a double slit is illuminated with a beam of a finite width, such as a Gaussian beam with a profile described by $E(r,z) \propto E_0\exp[-r^2/w(z)^2]$, the spatial position of the beam with respect to the slits can be recovered by observing the BSW directionality. BSWs excited by each slit will vary in amplitude with the lateral displacement between the centre of the beam and the double slit, resulting in a modified extinction ratio *R*. FDTD simulations of the relation between *R* and the lateral displacement is presented in Fig. 4a for the illumination with a Gaussian beam with a waist of 2.1 μm determined from the experiment (Fig. S6). The drastic change of *R* on both sides of the maximum value gives rise to a remarkable sensitivity of the directionality to deep-subwavelength displacements. This phenomenon can be well explained by the above described two-wave interference model. According to the Richards–Wolf diffraction integral,[50] for illumination under the focus of an objective with low NA, the field distribution will retain a Gaussian shape, and the phase will remain approximately invariant for a long range (4 μm in our case) of a transverse position. Consequently, the amplitudes of the BSWs excited by each slit can be considered as the illumination fields at the centers of the two slits: $E_{1e} = E_0\exp[-(x-x_1)^2/w_0^2]$, $E_{2e} = \gamma E_0\exp[-(x-x_2)^2/w_0^2]$, where x_1=−0.41 μm and x_2=0.345 μm are the centers of the slits, w_0=2.1 μm is the waist of the focused Gaussian beam, and γ is a ratio of the coupling efficiencies of each of the two slits. The and $\Delta\phi_\pi$ for destructive one. The parameters can be obtained as $\gamma = 1.09$, $\Delta\phi_0 = 0.13$ and $\Delta\phi_\pi = \pi - 0.067$ by fitting the numerical simulation curve to Eq. (1). The dependence on the lateral displacement calculated via Eq. (1) corresponds well to the FDTD simulations (Fig. 4a).

From Eq. (1), the variation of the extinction ratio for a tiny displacement δx can be estimated as

$$\delta R \approx \frac{4E_{1e}E_{2e}\sin\frac{\Delta\phi_\pi - \Delta\phi_0}{2}\sin\frac{\Delta\phi_\pi + \Delta\phi_0}{2}\frac{2(x_2-x_1)}{w_0^2}(E_{1e}^2 - E_{2e}^2)}{(E_{1e}^2 + E_{2e}^2 + 2E_{1e}E_{2e}cos\Delta\phi_\pi)^2}\delta x, \quad (2.)$$

For $E_{1e} = E_{2e}$, the value of δR approaches 0 for the conditions where *R* has maximum, which is determined by γ. On each side of the peak of *R*, there is a range of lateral positions where the slope of *R* is constant (Fig. S7), giving rise to the opportunity to detect subwavelength displacements within a significant linearity range. This average change in *R* can be defined as the sensitivity for displacement sensing through $S = \Delta R/\Delta x$ and observed over the displacement range from −450 to −350 nm and −200 to −100 nm with slopes of 2.888 ± 0.015 nm^{-1} and $-(2.817 \pm 0.009)$ nm^{-1} (Figs. 4b and c). Based on the linear dependence, the relative displacements Δ*x* can be estimated using the variation of *R* as $\Delta x = \Delta R/S$. The residual standard error of the linear fitting in Fig. 4b (Fig. 4c) is σ_R = 1.41 (1.69), demonstrating a limiting resolution of the displacement below 5 Å (6 Å) (see Methods). Since $\Delta\phi_\pi$ is responsible for destructive interference, it determines the slope as well as the half-width of *R* in terms of displacement, governing the sensitivity and linearity range of measurements. The increase (decrease) of the sensitivity leads to shorter (longer) linearity range. Therefore, asymmetric slits with different parameters can be designed for particular applications. The displacement sensing technique can

also be achieved utilizing TE-polarized BSW in a similar manner with properly designed multilayer and slits. It is worth noting that the use of a tightly focused Gaussian beam (NA=0.9 for example) will generate a Bessel profile of the incident field, which varies fast at the half-wavelength scales, resulting in complex *R* dependence with lateral position (Fig. S8). In addition, a tightly focused beam induces phase variation in the transverse plane. Both these factors reduce extinction ratio *R*. Despite this, it can also lead to the dramatic change of the *R* over narrow linearity range with the sensitivity, linearity range, shorter compared to the experimental value of 0.122 nm^{-1} sensitivity for 300 nm range. These differences are attributed to the imperfect shapes and smoothness of the fabricated multilayer and asymmetric slits (see Methods and Fig. S10 for details). Small fabrication tolerance of the slit parameters also makes influence on the sensitivity and linearity range for experimental measurements (see Methods and Fig. S11 for details). Therefore, the experimentally observed sensitivity has the potential to be increased with improved fabrication. The localization precision can also be increased by reducing noise in the signal detection system with the number of recorded

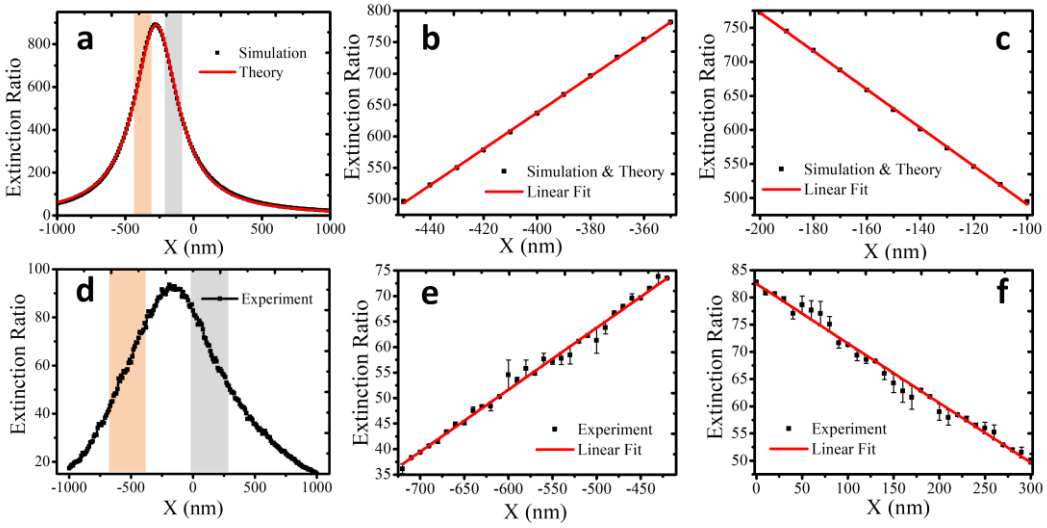

Fig. 4 Displacement sensing with the directional BSW**.** (a) Numerical (black rectangle) and analytical (red solid line) correspondence between R and the lateral displacement under illumination of a Gaussian beam (the waist radius is about 2.1 μm). (b-c) Linearity ranges in the area within orange and gray shadings in (a), respectively. The error bars correspond to the residual obtained from the linear fitting. (d-f) Experimental measurements of the relation between R and the lateral displacement and the linearity ranges on the two sides of the maximum value of R. The illumination wavelength is 600 nm.

and resolution being 0.34 nm^{-1}, 50 nm, and 0.7 nm, respectively.

To demonstrate the ultrasensitive displacement sensing experimentally, the sample was shifted with a step of 10 nm to change the relative position between the double slit and a Gaussian beam (NA=0.17, the waist radius after focusing is 2.1 μm). For the wavelength of 600 nm, a series of BFP images corresponding to different displacements were simulated and measured (Fig. S9). The relation between the extinction ratio *R* and the lateral position was obtained by processing each experimental BFP image. As shown in Fig. 4d, the maximum directionality is approximately 90 at the position of X=−150 nm. The extinction ratio exhibited a linear dependence on the displacement within a range of at least 300 nm from −720 nm to −420 nm and 0 to 300 nm (Fig. S7b), with sensitivity of 0.122 $\pm$ 0.002 nm^{-1} and – (0.11 $\pm$ 0.002) nm^{-1} in each linearity range, as well as the residual standard error of the linear fitting as 1.02 and 1.12. For comparison, in ultrasensitive optical metrology approaches using resonance nanoparticles, the maximum sensitivity was approximately 0.05 nm^{-1} for about a 50 nm linearity range[14-16]. Based on the linear dependence, the limiting relative displacement which determines the resolution of our approach can be estimated as approximately 8 nm and 10 nm, respectively.

The theoretical results (2.888 nm^{-1} sensitivity for 100 nm range) show higher sensitivity while the linearity range is individual images at each position. In the presented measurements, we captured 10 individual images at each position because the storage space of the camera was limited by the wide measurement range. Capturing 40 images at each position would allow reduction of the measurement error in *R* down to 0.1 with a resolution below 1 nm (see Methods for details).

Conclusions

We theoretically and experimentally demonstrated the efficient excitation of unidirectional BSWs by dielectric asymmetric nanoantennas. The unique dispersion properties of BSWs result in the large directional intensity extinction ratio and provide high sensitivity to illumination wavelength. Based on this directional effect, the interaction between the incident Gaussian beam and a double asymmetric slit enables high sensitivity to relative position and displacement between the slit and the illuminating free-space Gaussian beam or an optical fibre. The sensitivity as high as 2.888 nm^{-1} within a 100 nm range has been shown theoretically corresponding to approximately a 0.5 nm precision of the displacement measurements. The experimentally measured sensitivity is 0.122 nm^{-1} with a linearity range of 300 nm and approximately 8 nm resolution. While this demonstration has been achieved in 1D configuration, using a 2D arrangement of orthogonal slits, will

provide 2D displacement sensing capabilities, in a similar manner. The proposed technique may be applied to optical nanometrology, localization microscopy, atomic force microscopy, and lithography mask alignment and could also be extended to liquid environment. In addition, it can be used as an auxiliary means to correct the float of the scanner of AFMs, scanning tunneling microscopes, high-resolution fluorescence imaging and other equipment relying on precise positioning. For these applications, the developed approach can be used to compensate thermal and/or mechanical drifts of the samples and/or stages using the feedback signal linked to the changes of the extinction ratio *R*. Since drifts are particularly pronounced in fluid environments, parameters of the dielectric multilayer can be tuned in order to operate in liquid, which is essential for biologically relevant measurements. Apart from displacement sensing, the extinction ratio in the proposed configuration is also sensitive to the changes of the refractive index of the environment (see Methods and Fig. S12), which has potential applications in measuring, for example, the variations of a gas composition; multi-slit or hole configurations can be employed to decouple the signals related to refractive index changes and displacement for the development of integrated devices.

Methods

Sample fabrication and characterization. The dielectric multilayers were fabricated via plasma-enhanced chemical vapor deposition (PECVD) of SiO_2 and SiN_x on a standard microscope cover glass (0.17 mm thickness) at a vacuum <0.1 mtorr and temperature of 300 °C. Before the deposition, the cover glass was cleaned with acetone, piranha solution, ethyl alcohol, nanopure deionized water in sequence and dried with an N_2 stream. SiO_2 was used as the low (L) refractive index dielectric and SiN_x was used as the high (H) refractive index dielectric. Their thicknesses were 100 and 80 nm, respectively, and the refractive index of SiO_2 is n=1.46+i10^{-5}. The refractive index of SiN_x varies with the wavelength and was measured by ellipsometer (Sopra, Ges5e). The multilayer consists of 18 layers in total. The thickness of the top SiO_2 layer was 390 nm. The dielectric multilayer was characterized using transmission electron microscope (TEM, Bruker, JEM-2100F) and energy dispersive spectrometer (EDS). The dielectric multilayer was then coated with a gold film of 60 nm thickness by magnetron sputtering (Sputter-Lesker Lab 18), the gold film was then used to create asymmetric nanoslits by ion-milling in a helium ion microscope (HIM, Zeiss Orion). After the lithography, the gold film was removed with aqua regia and the dielectric multilayer was cleaned with acetone and, then, nanopure deionized water and dried with an N_2 stream. The detail morphology was characterized by atomic force microscope (AFM, Bruker, Dimension Icon). The length of the slits was 20 μm.

Optical Characterization. A leakage radiation microscope (LRM) was used for the BSW studies and metrology demonstration. A collimated laser beam (NKT supercontinuum laser) polarized perpendicularly to the slits was focused by a microscope objective (×10, numerical aperture NA = 0.3, by adjusting the size of the iris before the entrance pupil of the objective, the effective NA is about 0.17 and the waist radius of the Gaussian beam is 2.1 μm, as shown in Fig. S6). A series of bandpass filters with a FWHM of 10±2 nm and center wavelengths of 580±2, 600±2, 630±2, and 650±2 nm were used to investigate the sensitivity of the BSWs (Figs. S4d-g). The wavenumbers were derived to be 1.16k_0, 1.115k_0, 1.063k_0, and 1.022k_0 for the same wavelengths, respectively, which were consistent with the dispersion curve in Fig. 1b. The Gaussian beam was used to illuminate the asymmetric double slit etched on the top layer of the dielectric multilayer, which was positioned within the focal plane using a 3D piezo-stage (Physik Instrumente, P-545.3C8S). A polarizer and half-wave plate were used to change the polarization direction without altering the intensity. A second microscope objective (oil-immersion, ×100, NA, 1.49) below the substrate collected both the transmitted beam and excited BSW. A beam splitter was used to split the beam into two beams. Two lenses with different focus were used for the FFP imaging (Retiga camera, Qimaging, America) and BFP imaging (Neo-sCMOS camera, Andor, UK). Additionally, a white source was expanded by a lens and tightly focused onto the dielectric multilayer from the bottom side of the substrate to capture the reflected BFP.

The numerical filtration of the incident Gaussian beam and other scattered light in the BFP images was performed in two steps. Firstly, the background noise (dark noise of the CCD) was subtracted from the recorded BFP images in Fig. S4b. The background is acquired by capturing a BFP in the absence of the sample. The processed image was used for the evaluation of the extinction ratio by integrating the BSW intensity within the defined area (Fig. 3e). To demonstrate the directional imbalance of the BSW signal visually, the second filtration was performed. The incident Gaussian beam and other scattered light was numerically removed by limiting the wave vector of the detected light within the region of $\left|k_{\parallel}/k_0 - n_{eff}\right| \leq 0.03$ in *k*-space, which is around the effective index of the BSW, resulting in Fig. S4c. The second step has no effect on the value of extinction ratio.

To demonstrate the ultrasensitive displacement sensing, the sample was shifted with a step of 10 nm to change the relative position between the slit and the illuminating Gaussian beam. The corresponding BFP images were captured for each position. In consideration of the instability of the experimental setup and environment, 10 individual images were captured at each position and averaged. It is worth mentioning that with increasing number of images acquired at each position, the curve accuracy increases.

Deviation between experimental and simulated extinction ratios due to fabrication uncertainties. The multilayer is fabricated via plasma-enhanced chemical vapor deposition (PECVD). The roughness and drift of thickness over the sample area is accumulated with the increase of number of layers (Fig. S3a). As a consequence, the illuminating beam is not everywhere strictly normal to the sample surface (Fig. S5a). We simulated the wavelength dependence of the directional BSW excitation for different tilt angles from the normal (Figs. S5c and d). The results show a dramatic change in the magnitude of extinction ratio with a perceived tilt. This in turn leads to the changes in the displacement sensing performance (Figs. S10a

and b). Taking into account the experimentally roughness of the sample surface, the simulated directional BSW excitation compares well with the experimental results. The distinct variation on *R* for small tilt angles can be understood by Eq. (1). Since $\Delta\phi_\pi$ is responsible for destructive interference, it determines the magnitude of *R* in terms of wavelength and displacement. The tilt of the incident beam causes a wavefront curvature of the illuminating field on the two slits, resulting in the variation of $\Delta\phi_0$ and $\Delta\phi_\pi$ in Eq. (1) and, therefore, giving rise to the dramatic change in the extinction ratio.

The shape of the fabricated slits is trapezoidal as characterized by atomic force microscopy (Figs. S3f and g), deviating from the ideal rectangular shapes considered in the simulations (Fig. 3i). Taking into account the experimentally measured size and shape of the nanoslits, the simulated directional BSW excitation compares well with the experimental results (Figs. S5b and e). In turn, the displacement sensing performance is influenced by the shape of the nanoslits (Fig. S10c).

The sensitivity and linearity range for different slit parameters is shown in Fig. S11, demonstrating a small fabrication tolerance to keep the same order of magnitude than that of the simulation result in Fig. 4(a). This can be explained from Eq. 2 that the extinction ratio and sensitivity are governed by the destructive interference, which is determined by the coupling efficiency and phase of BSW. From Figs. 1(d) and (e), the coupling efficiency and phase are sensitive to the slit parameters. Hence, the sensitivity will be decreased as the width or depth takes a tiny modulation on the optimized parameters, which makes influence on the sensitivity and linearity range for experimental measurement.

Resolution of displacement. The residual standard error of the linear fitting for the extinction ratio in the linearity range can be expressed as $\sigma_R = \sqrt{\frac{1}{N}\sum_{i=1}^{N}\epsilon_i^2}$, where *N* is the number of fitting points, ε_i is error of extinction ratio between the original data and linear fitting for each point (error bar in Figs. 4b-c and e-f in main text). The limitation of distinguishable variation of *R* can be regarded as σ_R. The fitting line has its slope *S* and standard error σ_S. Considering both the error in extinction ratio and slope, the lateral displacement resolution can be estimated as $\Delta x = \frac{\sigma_R}{S} \pm \frac{\sigma_R \sigma_S}{S^2 - \sigma_S^2}$.

Estimation of measurement errors. Using an error propagation formula, the error in obtaining extinction ratio can be expressed as $\frac{\sigma_R}{R} = \sqrt{\left[\frac{\sigma_N}{I_r}\right]^2 + \left[\frac{\sigma_N}{I_l}\right]^2}$, where *R* is the extinction ratio, I_r and I_l are the measured intensities along the $+x$ and $-x$ axis, σ_N is the mean uncertainty of camera noise in collecting the BFP. In the case of a high extinction ratio ($I_r >> I_l$), the error can be approximated as $\sigma_R \approx R^2\sigma_N / I_r$. After the background noise has been subtracted for each image, which is between 100-200 counts, an uncertainty due to the camera noise is about σ_N =20 for each measurement. The uncertainty of the camera noise can be mitigated by increasing the number of individual images measured at each position. The intensity of I_r in the case of the constructive interference along the $+x$ axis for the experimental conditions is approximately 5×10^4 counts. In order to obtain the uncertainty of *R* below 0.1, more than 40 individual images should be measured.

Refractive index sensing based on directional imbalance of BSWs. The wave vector of the BSW mode is sensitive to the refractive index of a surrounding medium. Consequently, if the refractive index of the superstrate changes, the wave vector of the excited BSW will change resulting in the changes of the coupling efficiency and phase of the scattered BSWs by the double slit. Therefore, the original constructive and destructive interference will be influenced, leading to the modified extinction ratio. We simulated the dependence of *R* on a refractive index of the superstrate under illumination with a Gaussian beam (the waist radius is about 2.1 μm) for a fixed wavelength (600 nm) and fixed position (Fig. S12). Dramatic changes were observed for miniscule changes of the refractive index with a sensitivity D*R*/Dn ≈ 6900/RIU in the linearity range (Fig. S12b). This high sensitivity for refractive index sensing can be used to measure the changes of the gas concentration, such as hydrogen or CO_2 with high precision. The multilayer can be designed for the use also in liquid environments.

Author Contributions

R.W. and X.L. developed the concept of the work; X.L. carried out the analytical and numerical modelling; R.W., L.D. and X.Y designed the experiments; R.W. and X.W. prepared the sample; R.W. performed the experiments; R.W., X.L. and A.V.Z. wrote the manuscript; Y.J., A.W. and A.V.Z. analysed the results; L.D., A.W., A.V.Z. and X.Y. supervised the project; all authors discussed the results and commented on the final manuscript. R.W. and X.L. contributed equally to this work.

Conflicts of interest

There are no conflicts of interest to declare.

ACKNOWLEDGEMENTS

This work was supported by Youth Innovation Promotion Association CAS (2021232), National Science Foundation of China (61905269, 62005305), Shanghai Sailing Program (19YF1456600,18YF1428200, 20YF1456800) and the Open Research Fund of State Key Laboratory of Transient Optics and Photonics. L.D acknowledges the support given by Guangdong Special Support Program. A.V.Z. acknowledges support from EPSRC (UK) and the ERC iCOMM project (789340).

Notes and references

1. B. P. Abbott, R. Abbott, T. D. Abbott, M. R. Abernathy, F. Acernese, K. Ackley, C. Adams, T. Adams, P. Addesso, R. X. Adhikari, *Phys Rev Lett*, 2016, **116**, 061102.
2. T. Heyduk, *Current Opinion in Biotechnology*, 2002, **13**, 292-296.
3. E. Betzig, G. H. Patterson, R. Sougrat, O. W. Lindwasser, S. Olenych, J. S. Bonifacino, M. W. Davidson, J. Lippincott-Schwartz and H. F. Hess, *Science*, 2006, **313**, 1642.

4. A. Yildiz, J. N. Forkey, S. A. McKinney, T. Ha, Y. E. Goldman and P. R. Selvin, *Science*, 2003, **300**, 2061.
5. A. A. Deniz, M. Dahan, J. R. Grunwell, T. Ha, A. E. Faulhaber, D. S. Chemla, S. Weiss and P. G. Schultz, *Proceedings of the National Academy of Sciences*, 1999, **96**, 3670.
6. P. Segovia, G. Marino, A. V. Krasavin, N. Olivier, G. A. Wurtz, P. A. Belov, P. Ginzburg and A. V. Zayats, *Opt Express*, 2015, **23**, 30730-30738.
7. L. Carletti, G. Marino, L. Ghirardini, V. F. Gili, D. Rocco, I. Favero, A. Locatelli, A. V. Zayats, M. Celebrano, M. Finazzi, G. Leo, C. De Angelis and D. N. Neshev, *ACS Photonics*, 2018, **5**, 4386-4392.
8. N. Bobroff, *Measurement Science and Technology*, 1993, **4**, 907-926.
9. S. J. A. G. Cosijns, H. Haitjema and P. H. J. Schellekens, *Precision Engineering*, 2002, **26**, 448-455.
10. L. Wei, A. V. Zayats and F. J. Rodriguez-Fortuno, *Phys Rev Lett*, 2018, **121**, 193901.
11. C. Sonnichsen, B. M. Reinhard, J. Liphardt and A. P. Alivisatos, *Nat Biotechnol*, 2005, **23**, 741-745.
12. P. Nordlander and E. Prodan, *Nano Letters*, 2004, **4**, 2209-2213.
13. G. H. Yuan and N. I. Zheludev, *Science*, 2019, **364**, 771-775.
14. S. Roy, K. Ushakova, Q. van den Berg, S. F. Pereira and H. P. Urbach, *Phys Rev Lett*, 2015, **114**, 103903.
15. Z. Xi, L. Wei, A. J. Adam, H. P. Urbach and L. Du, *Phys Rev Lett*, 2016, **117**, 113903.
16. T. Zang, H. Zang, Z. Xi, J. Du, H. Wang, Y. Lu and P. Wang, *Phys Rev Lett*, 2020, **124**, 243901.
17. L. Du, A. Yang, A. V. Zayats and X. Yuan, *Nature Physics*, 2019, **15**, 650-654.
18. F. López-Tejeira, S. G. Rodrigo, L. Martín-Moreno, F. J. García-Vidal, E. Devaux, T. W. Ebbesen, J. R. Krenn, I. P. Radko, S. I. Bozhevolnyi, M. U. González, J. C. Weeber and A. Dereux, *Nature Physics*, 2007, **3**, 324-328.
19. C. P. McPolin, J. S. Bouillard, S. Vilain, A. V. Krasavin, W. Dickson, D. O'Connor, G. A. Wurtz, J. Justice, B. Corbett and A. V. Zayats, *Nat Commun*, 2016, **7**, 12409.
20. A. Baron, E. Devaux, J. C. Rodier, J. P. Hugonin, E. Rousseau, C. Genet, T. W. Ebbesen and P. Lalanne, *Nano Lett*, 2011, **11**, 4207-4212.
21. W. Yao, S. Liu, H. Liao, Z. Li, C. Sun, J. Chen and Q. Gong, *Nano Lett*, 2015, **15**, 3115-3121.
22. J. S. Liu, R. A. Pala, F. Afshinmanesh, W. Cai and M. L. Brongersma, *Nat Commun*, 2011, **2**, 525.
23. F. J. Rodríguez-Fortuño, G. Marino, P. Ginzburg, D. O'Connor, A. Martínez, G. A. Wurtz and A. V. Zayats, *Science*, 2013, **340**, 328.
24. J. Lin, J. P. Mueller, Q. Wang, G. Yuan, N. Antoniou, X. C. Yuan and F. Capasso, *Science*, 2013, **340**, 331-334.
25. P. Yeh, A.Yariv and C. S. Hong, *J. Opt. Soc. Am.*, 1977, **67**, 423-438.
26. B. Qiang, A. M. Dubrovkin, H. N. S. Krishnamoorthy, Q. Wang, C. Soci, Y. Zhang, J. Teng and Q. J. Wang, *Advanced Photonics*, 2019, **1**, 26001-26001.
27. D. A. Shilkin, E. V. Lyubin, I. V. Soboleva and A. A. Fedyanin, *Opt. Lett.*, 2015, **40**, 4883-4886.
28. R. Wang, Y. Wang, D. Zhang, G. Si, L. Zhu, L. Du, S. Kou, R. Badugu, M. Rosenfeld, J. Lin, P. Wang, H. Ming, X. Yuan and J. R. Lakowicz, *ACS Nano*, 2017, **11**, 5383-5390.
29. W. M. Robertson and M. S. May, *Applied Physics Letters*, 1999, **74**, 1800-1802.
30. M. Liscidini, and J. E. Sipe, *Journal of the Optical Society of America B*, 2009, **26**, 279-289.
31. A. Sinibaldi, E. Descrovi, F. Giorgis, L. Dominici, M. Ballarini, P. Mandracci, N. Danz and F. Michelotti, *Biomed Opt Express*, 2012, **3**, 2405-2410.
32. V. Koju and W. M. Robertson, *Sci Rep*, 2017, **7**, 3233.
33. D. Ge, J. Shi, A. Rezk, C. Ma, L. Zhang, P. Yang and S. Zhu, *Nanoscale Res Lett*, 2019, **14**, 319.
34. G. Lerario, A. Cannavale, D. Ballarini, L. Dominici, M. D. Giorgi, M. Liscidini, D. Gerace, D. Sanvitto and G. Gigli, *Opt. Lett.*, 2014, **39**, 2068-2071.
35. T. Sfez, E. Descrovi, L. Dominici, W. Nakagawa, F. Michelotti, F. Giorgis and H.-P. Herzig, *Applied Physics Letters*, 2008, **93**, 061108.
36. R. Wang, J. Chen, Y. Xiang, Y. Kuai, P. Wang, H. Ming, J. R. Lakowicz and D. Zhang, *Phys Rev Appl*, 2018, **10,** 024032.
37. U. Stella, L. Boarino, N. De Leo, P. Munzert and E. Descrovi, *ACS Photonics*, 2019, **6**, 2073-2082.
38. A. Angelini, E. Barakat, P. Munzert, L. Boarino, N. De Leo, E. Enrico, F. Giorgis, H. P. Herzig, C. F. Pirri and E. Descrovi, *Sci Rep*, 2014, **4**, 5428.
39. M. Menotti and M. Liscidini, *Journal of the Optical Society of America B*, 2015, **32**, 431-438.
40. M.-S. Kim, B. Vosoughi Lahijani, N. Descharmes, J. Straubel, F. Negredo, C. Rockstuhl, M. Häyrinen, M. Kuittinen, M. Roussey and H. P. Herzig, *ACS Photonics*, 2017, **4**, 1477-1483.
41. M. Wang, H. Zhang, T. Kovalevich, R. Salut, M.-S. Kim, M. Suarez, M.-P. Bernal, H.-P. Herzig, H. Lu and T. Grosjean, *Light: Science & Applications*, 2018, **7**, 1-8.
42. X. Lei, Y. Ren, Y. Lu and P. Wang, *Physical Review Applied*, 2018, **10,** 044032.
43. P. Lalanne, J. P. Hugonin and J. C. Rodier, *Phys Rev Lett*, 2005, **95**, 263902.
44. H. W. Kihm, K. G. Lee, D. S. Kim, J. H. Kang and Q. H. Park, *Applied Physics Letters*, 2008, **92**, 051115.
45. P. Lalanne, J. P. Hugonin, and J. C. Rodier, *J. Opt. Soc. Am. A*, 2006, **23**, 1608-1615.
46. X. Li, Q. Tan, B. Bai and G. Jin, *Applied Physics Letters*, 2011, **98**, 251109.
47. J. S. Bouillard, S. Vilain, W. Dickson, G. A. Wurtz and A. V. Zayats, *Sci Rep*, 2012, **2**, 829.
48. E. Descrovi, E. Barakat, A. Angelini, P. Munzert, N. De Leo, L. Boarino, F. Giorgis and H. P. Herzig, *Opt. Lett.*, 2013, **38**, 3374-3376.
49. A. Angelini, E. Enrico, N. De Leo, P. Munzert, L. Boarino, F. Michelotti, F. Giorgis and E. Descrovi, *New Journal of Physics*, 2013, **15**, 073002.
50. B. Richards and E. Wolf, *Proceedings of the Royal Society of London. Series A. Mathematical and Physical Sciences*, 1959, **253**, 358-379.